

Toward High-Speed Nanoscopic Particle Tracking via Time-Resolved Detection of Directional Scattering

Paul Beck, Martin Neugebauer, and Peter Banzer*

Owing to their immediate relevance for high precision position sensors, a variety of different sub-wavelength localization techniques has been developed in the past decades. However, many of these techniques suffer from low temporal resolution or require expensive detectors. Here, a method is presented that is based on the ultrafast detection of directionally scattered light with a quadrant photodetector operating at a large bandwidth, which exceeds the speed of most cameras. The directionality emerges due to the position dependent tailored excitation of a high-refractive index nanoparticle with a tightly focused vector beam. A spatial resolution of 1.1 nm and a temporal resolution of 8 kHz is reached experimentally, which is not a fundamental but rather a technical limit. The detection scheme enables real-time particle tracking and sample stabilization in many optical setups sensitive to drifts and vibrations.

In general, spatial and temporal resolution are usually limited by technical aspects of the corresponding techniques, such as camera frame rates or similar.

Here, we combine concepts of the fast detection methods utilized in trapping experiments with an easy-to-operate particle-on-substrate arrangement. The localization principle is based on the position-dependent directional scattering by a dielectric nanoparticle, resulting from the tailored excitation with a tightly focused vector beam.^[15–17] The directionality results from interfering magnetic and electric dipole moments excited in the particle. This method has been already demonstrated in previous (low-speed) position sensing experiments,

1. Introduction

In the past, multiple approaches for the localization of single nanoparticles or multi-particle structures have emerged from the growing interest in ultra-precise positioning techniques for nanometrological applications.^[1] These include scanning probe microscopy, which always involves a probe tip placed close to the sample,^[2] but also all-optical solutions that aim to go beyond the diffraction limit, such as fluorescence microscopy approaches,^[3–7] camera-based interferometric detection of light scattered by a particle, utilizing the diffraction-limited optical image of a point-like emitter,^[8–11] photodetector-based localization of a particle in an optical trap^[12,13] or via detection of the total intensity of scattered light with two separate detectors.^[14]

proving the capability of this scheme to provide ultra-high spatial resolution in the sub-Angström regime.^[18–21] However, the detection scheme in these experiments relies on a CCD camera, making it difficult to reach high temporal resolution while keeping the costs for the detection low.


In the present study, we enhance the temporal resolution of the technique by detecting the scattered light with a quadrant photodetector (QPD). This allows for a tremendous increase in detection speed, while the spatial resolution of the detection is comparable to recent experiments.^[18–22] This fast, high-precision particle tracking can be directly employed as a stabilization mechanism via a suitable feedback loop-based approach.

2. Theoretical Concept

The underlying idea enabling precise localization is based on position-dependent directional scattering from a dielectric nanoparticle upon tailored excitation with unconventional electromagnetic fields. This directionality in scattering is centered around an effect originally described by Kerker^[23] who showed that the superposition of the emission of transverse and orthogonally aligned electric and magnetic dipole moments, excited by a linearly polarized plane wave in a particle, can lead to a strong forward-backward asymmetry of the scattering. This phenomenon is usually referred to as Kerker scattering or Huygens dipole.^[24–27] A scatterer featuring non-zero electric and magnetic polarizabilities is required to observe this effect.^[28,29] For such a scatterer, the spectral positions of dipole resonances are linked to the particle size. However, the aforementioned scheme of plane-wave excitation is obviously not suited for encoding position information of the scatterer relative to the excitation field in the

P. Beck, Dr. M. Neugebauer, Dr. P. Banzer
Max Planck Institute for the Science of Light
Staudtstr. 2, D-91058 Erlangen, Germany
E-mail: peter.banzer@mpl.mpg.de

P. Beck, Dr. M. Neugebauer, Dr. P. Banzer
Institute of Optics, Information and Photonics
Department of Physics
Friedrich-Alexander-University Erlangen-Nuremberg
Staudtstr. 7/B2, D-91058 Erlangen, Germany

 The ORCID identification number(s) for the author(s) of this article can be found under <https://doi.org/10.1002/lpor.202000110>

© 2020 The Authors. Published by Wiley-VCH GmbH. This is an open access article under the terms of the Creative Commons Attribution-NonCommercial License, which permits use, distribution and reproduction in any medium, provided the original work is properly cited and is not used for commercial purposes.

DOI: 10.1002/lpor.202000110

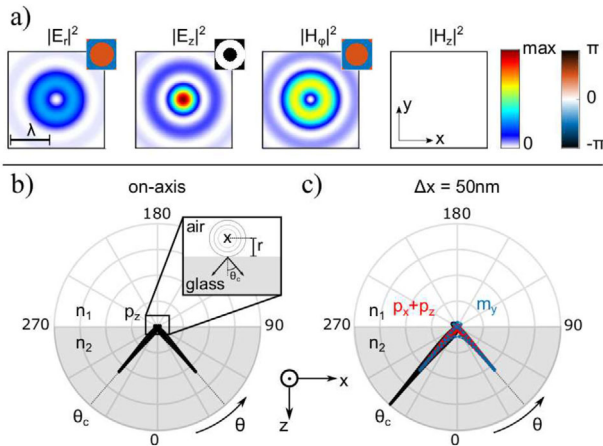


Figure 1. a) Focal electric and magnetic energy density distributions for a radially polarized beam tightly focused by a microscope objective with numerical aperture (NA) of 0.9. The fields are split into transverse (E_r , H_ϕ) and longitudinal (E_z , H_z) components. The insets show the relative phases of each component respectively. The focal plane (xy) is shown. A square area of side length $2.4\lambda = 1.52 \mu\text{m}$ is shown. The plots are normalized to the maximum value of the total field intensity $I_{\text{tot}} = |E|^2 + |H|^2$ in Gaussian units. b), c) Analytically calculated emission patterns of a dipolar emitter sitting above an interface (grey) excited by the local fields of a tightly focused radially polarized beam. The plots show the emission pattern in the x - y plane depending on the emission angle θ ($^\circ$). The upper half-space consists of air with a refractive index $n_1 = 1$, whereas the lower half-space (grey) is filled with glass (substrate) with $n_2 = 1.5$. The inset in b) shows the scatterer modelled analytically as a point dipole (small cross) with distance r (particle radius) to the surface. b) Emission pattern for the dipole being placed on the optical axis, c) for the scatterer being displaced by $\Delta x = 50$ nm away from the optical axis. The interference of electric ($p_x + p_z$, red) and transverse magnetic (m_y , blue) dipole emission leads to strongly directional scattering (black, total emission pattern).

observed directional scattering effect. In order to facilitate Kerker scattering for localization, position dependent particle-light interaction is crucial. This way, the scattering pattern varies for a displacement of the scatterer with respect to the excitation field, which is not the case in the scheme envisioned originally by Kerker. This can be achieved by tailored excitation with, for example, a tightly focused radially polarized beam. Such fields exhibit unconventional and striking features, such as a strong longitudinal electric field component E_z at the center^[15,16] and an azimuthal magnetic (H_ϕ) as well as a radial electric field component (E_r) for off-axis positions.^[30] In addition, the focal spot exhibits cylindrical symmetry. The normalized focal electric and magnetic energy density distributions and the corresponding relative phases, calculated using vectorial diffraction theory^[31] are shown in **Figure 1a**.

In first approximation, the focal fields exhibit a linear dependence for a region of $r \ll \lambda$, that is, close to the optical axis^[18]:

$$\mathbf{E}(x, y) \propto xE_x^0 \mathbf{e}_x + yE_y^0 \mathbf{e}_y + iE_z^0 \mathbf{e}_z \quad (1)$$

$$\mathbf{H}(x, y) \propto -yH_x^0 \mathbf{e}_x + xH_y^0 \mathbf{e}_y. \quad (2)$$

Here, we also take into account the relative phase difference of $\pi/2$ between the transverse and longitudinal components.^[32,33] The non-uniform energy density distributions together with the

beam-inherent symmetry and phase differences offer an excellent tool for the tailored excitation of a dielectric nanoparticle, which supports both electric and magnetic dipole resonances. If such a particle with a diameter smaller than the focal spot is placed in the described fields, the dipole moments $\mathbf{p} \propto \mathbf{E}$ and $\mathbf{m} \propto \mathbf{H}$ are excited,^[34,35] besides smaller contributions by higher-order modes. Amplitude and phase of the dipole moments strongly depend on the local fields.^[36] Accordingly, a scan of the nanoparticle across the focus results in a superposition of a longitudinal electric (p_z) and transverse magnetic (m_x , m_y) dipole moments, together with minor contributions of transverse electric dipole moments (p_x , p_y). The latter ones can be neglected here for several reasons. First, the longitudinal electric field component of the excitation field is noticeably stronger than the transverse one in the region of interest. Second, the excitation wavelength of 630 nm is closer to the magnetic dipolar resonance, and hence m_x and m_y are excited much more efficiently than p_x and p_y . A third reason is directly linked to the far-field emission of the individual dipole moments (for more details see ref. [18]). The interference of the emission of longitudinal and transverse dipole moments results in a total emission pattern yielding a strong transverse directionality, which depends on the relative amplitudes and phases of the excited resonances and therefore on the local fields. For the analytical calculations of the dipole emission patterns shown in **Figure 1**, we take into account the experimental parameters for a silicon sphere of diameter 156 nm, coated with a 6 nm oxide shell, placed on a glass substrate ($n_2 = 1.5$). We assume local excitation by the fields shown in **Figure 1a**. Relative phases and amplitudes follow from numerical calculations of the particle and the given excitation field. In the analytical calculation, we further approximate the distance of the point-like dipoles with respect to the substrate by the total particle radius of $r = 84$ nm, including the SiO_2 shell. The resulting far-field patterns are shown in **Figures 1b,c**, which correspond to the cases of a particle on the optical axis (b) and for a displacement of 50 nm in positive x direction (c). The local electromagnetic fields induce the dipole moments $p_x = p_y = 0$, $p_z = 0.2487 + i0.1345$ (electric), $m_x = m_y = m_z = 0$ (magnetic) for on-axis position and $p_x = 0.0226 + i0.0417$, $p_y = 0$, $p_z = -0.2408 + i0.1302$, $m_x = 0$, $m_y = -0.1147 + i0.0657$, $m_z = 0$ for $\Delta x = 50$ nm. Due to the close proximity of the scatterer to the interface, the near-fields are evanescently coupled to the glass substrate. Within the substrate, the scattered light is dominantly directed along the angle of total internal reflection θ_c , with $\theta_c = 41.8^\circ$ for the given refractive indices and wavelength of the emitted light. The coupling as well as the approximation of the particle as a point dipole with distance r (particle radius) to the substrate are illustrated in the inset in **Figure 1b**. The overcritical angular range corresponds to transverse wavevectors $k_t = (k_x^2 + k_y^2)^{1/2} \geq k_0$, where $k_0 = 2\pi/\lambda$ is the vacuum wavenumber. We notice that for an on-axis particle position, only a longitudinal electric dipole moment p_z is excited, resulting in symmetric scattering with respect to the optical axis (see the two equally strong peaks at the critical angle). In contrast, for an off-axis position depicted in **Figure 1c**, the superposition of p_x , p_z , and m_y dipole components yields a highly asymmetric pattern (pronounced lateral scattering). As mentioned before, the asymmetry is dominated by the interference of p_z and m_y . In conclusion, the position of the particle relative to the beam is encoded in the observed directionality of the scattered light. Experimentally, the angular emission

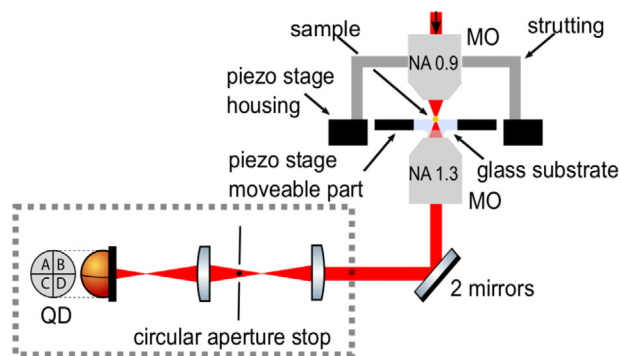


Figure 2. Lower part of the experimental setup with the analysis section highlighted by the grey dotted box. The incoming radially polarized mode is tightly focused by the upper NA = 0.9 microscope objective (MO). The silicon nanoparticle is placed in the focal plane with a 3D piezo positioning stage. After interaction with the sample, the light is collected by a NA = 1.3 oil-immersion MO in order to collect the scattered light also in an angular range beyond that of the incoming beam in the range $0.9 \leq \text{NA} \leq 1.3$. In order to detect only light emitted into the above mentioned overcritical angular range, the inner part of the beam is blocked by placing a circular aperture stop in the plane of an intermediate BFP image. This intermediate image plane is again imaged onto a conventional quadrant photodetector (QD) in order to measure the directionality of the angular emission spectrum.

spectrum can be accessed by imaging the back focal plane (BFP) of a high-NA immersion-type collecting microscope objective (MO). The implementation of BFP imaging will be discussed in the following. We will show in the following that the actual experimental detection and analysis of the BFP data can also be done with a quadrant photodetector rather than a camera, which offers high-speed capabilities.

3. Implementation

For the experimental implementation (see **Figure 2**) of the aforementioned excitation scheme we use a setup similar to the one described in refs. [19, 32, 36]. However, the detection part of the setup has been modified substantially to enable a high temporal resolution in the tracking of individual nanoparticles.

We first generate a collimated radially polarized doughnut mode using a tunable q-plate.^[37] The beam (HeNe laser with a wavelength of 633 nm) is tightly focused by a microscope objective with an NA of 0.9 onto the silicon nanoparticle, which was deposited on a glass substrate ($n_2 = 1.5$) using a custom AFM-in-SEM-based manipulation system.^[38] The silicon sphere has a diameter of 156 nm with a silicon oxide shell of approximately 6 nm. The glass substrate is mounted on a 3D piezo positioning stage, which allows for moving the sample precisely with respect to the focal spot. In this experiment, we aimed for a very compact and mechanically stable construction in order to also detect small-amplitude vibrations in this proof-of-concept study. In contrast to other setups utilized before, we include a very rigid metal rail construction, which connects all components for the preparation of the incoming beam. The rail itself is fixed to the holder of the upper microscope objective and the frame of the piezo stage. After interaction of the focused beam with the sample, the scat-

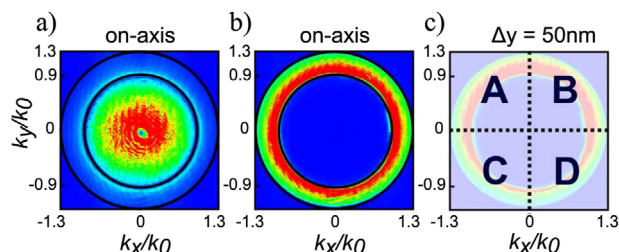


Figure 3. False-color BFP images. For these images, the QD has been replaced by a CCD camera, with the detection plane at the same position. a) Image of the full BFP for on-axis particle position, yielding a symmetric emission pattern. The coordinate system and the black circles indicate the different angular ranges. b) BFP image for the same particle position. The angular range $k_t/k_0 < 0.9$ is blocked by the aperture stop inserted in the intermediate image. c) Schematic depiction of the size of the BFP image with respect to the quadrant detector. The image was recorded for a relative particle displacement of $\Delta y = 50$ nm from the optical axis, leading to a highly asymmetric power distribution on the detector.

tered and transmitted light is collected with an oil-immersion microscope objective of NA = 1.3. The part of the light not interacting with the particle will be observed in an angular range within a solid angle corresponding to $\text{NA} \leq 0.9$ only. Only light scattered by the particle can enter an angular range beyond this solid angle. By imaging the back focal plane (BFP) of the collection MO with an additional lens, we can access k -space and, thus, the angularly resolved scattering of the particle and transmission of the incoming beam through the sample. In previous low-speed position-sensing experiments^[18,19,32] the BFP was analyzed with a spatially resolving detector (camera). By using a camera, light scattered and transmitted into the range below the illumination NA and light scattered into a range beyond including the supercritical angular range can be easily distinguished from each other. For illustration, **Figure 3a** shows a BFP image recorded post-measurement with a camera for a particle position on the optical axis, yielding symmetric scattering. In the post-processing, only the overcritical angular range with $k_t/k_0 > 1$ (i.e., $\text{NA} > 0.9$) is taken into account. The actual particle position was encoded in a differential signal between light scattered along positive and negative k_x or k_y direction. Here, we now extend this Kerker scattering based localization method to the high-speed regime by using a quadrant photodiode as a detector instead and by running a time and frequency-resolved analysis. We prove that even without high spatial resolution of the detector, we can measure the scattering directivity and localize a nanoparticle with high precision coming close to previously reported values,^[18,19,32] but with much higher temporal resolution. The latter can be achieved easily, because even basic photodetectors typically operate at bandwidths of a few 100 kHz, whereas such detection speed is hardly achievable with cameras. However, it is important to note that the scheme proposed here can only provide high spatial localization precision if the BFP to be imaged onto the quadrant photodetector is spatially filtered, in order to take into account the angular range $\text{NA} \geq 0.9$, where only scattered light is present. In the experiment, we first image the BFP of the lower MO onto a circular aperture stop (see **Figure 2**), matched in dimensions such that the angular range $\text{NA} < 0.9$ is blocked before imaging it onto the detector. By doing so, the central region of the image

is blocked, as shown in Figure 3b. In order to illustrate the position and orientation of the image with respect to the quadrant detector and the influence of a particle displacement, we show an exemplary BFP camera image for a particle displacement of $\Delta y = 50$ nm (Figure 3c). The quadrants are labeled by A, B, C, and D. The asymmetry of the intensity distribution reveals the strong position dependence of the scattering pattern. In order to quantitatively analyze the position dependent asymmetry of the power distribution in the BFP image on the quadrant photodetector, we define so-called directivity parameters similar to the ones employed for camera measurements.^[18–20,32] The four quadrants of the detector integrate the respective intensity distributions. Hence, we define the directivity parameters as differential and normalized signals for the chosen orientation of the quadrants with respect to the coordinate system indicated in Figure 3:

$$D_x = \frac{(P_A + P_C) - (P_B + P_D)}{P_A + P_B + P_C + P_D}, \quad (3)$$

$$D_y = \frac{(P_A + P_B) - (P_C + P_D)}{P_A + P_B + P_C + P_D}. \quad (4)$$

Here, P_A, \dots, P_D denote the integrated intensity distribution, i.e., the optical power measured by each individual quadrant. With this definition, a symmetric scattering pattern (on-axis particle position) leads to $D_x = D_y = 0$, which can be used as a reference position, whereas an uneven power distribution results in nonzero values depending on the particle position. In order to relate the experimental directivity values to the actual particle position, we choose a suitable calibration procedure similar to the one employed in ref. [18–21]. To this end, we scan the particle across the focal fields in an area of $200 \text{ nm} \times 200 \text{ nm}$ around the optical axis in steps of 20 nm while measuring and evaluating parameters D_x and D_y at each point of the scan. The aforementioned linearity of the focal fields in the region $r \ll \lambda$, as described by Equations (1) and (2) translates to the directivity parameter. Accordingly, it is possible to fit planes $D_x(x, y)$ and $D_y(x, y)$ to the measured calibration data and combine them into a single matrix equation. The obtained relation can now be inverted in order to retrieve the particle position $x(D_x, D_y)$, $y(D_x, D_y)$ from the experimental directivity values. An example of such a calibration plane for $D_x(x, y)$, together with the measurement data it is based on, is shown in Figure 4. Such a calibration is performed prior to every individual measurement in order to also account for slight changes in the beam profile over time that might occur due to drifts of beam-shaping optical components.

4. Experimental Section

As a first step and in order to quantitatively verify the precision of the measurement technique described above, the built-in capacitive position sensor of the piezo stage was utilized to measure the particle position, while simultaneously recording it using the optical reconstruction method. Despite the fact that the optical approach will outperform the capacitive one in spatial and temporal resolution, this cross-check is ideal for a preliminary verification of the method. Furthermore, the optical approach inherently measures the actual position of the particle relative to

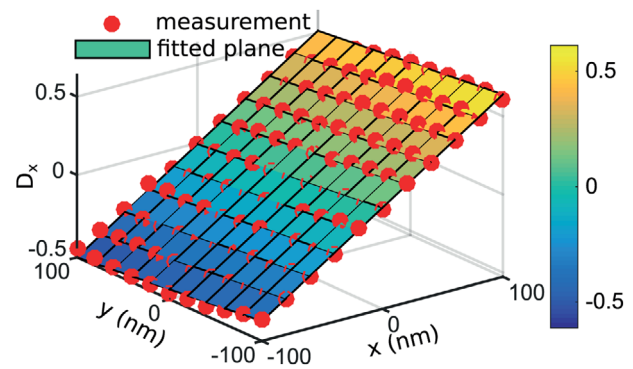


Figure 4. Employed calibration technique. The particle is scanned through a rectangular area of $200 \text{ nm} \times 200 \text{ nm}$ around the optical axis in the focal plane in steps of 20 nm and the parameters D_x and D_y are computed for each position. The plot shows the experimentally obtained directivity values (red dots) for each particle position and the $D_x(x, y)$ planar fit. The very good agreement of fit and measurement data confirms the expected linear dependence of the directivity parameters.

the illumination and not just relative to the origin of the stage's coordinate origin, which can have advantages when applied in real-world systems. For demonstration, the oscillation of the particle on its substrate was measured by inducing a 700 Hz vibrational frequency with an external loudspeaker placed close to the setup. This frequency is well below the detector bandwidth and thus easily detectable. Figure 5a shows the overlay of the time-resolved one-dimensional particle position $x(t)$ resulting from the optical position reconstruction (blue) and the corresponding position data recorded by the piezo stage (red). The two datasets were in very good agreement with each other. However, it was apparent that the oscillation amplitudes (maximum particle displacement) differed for both approaches. Also, the reconstructed position data were subject to a lower-frequency modulation. For further analysis, the Fourier spectrum of the time-resolved signals shown in Figure 5a was computed in order to extract the most prominent oscillation frequencies. The low-frequency range of the resulting spectra, computed using a fast Fourier transform (FFT) algorithm,^[39] are shown in Figure 5b, confirming the good agreement already observed in the position data. However, the 700 Hz oscillation is more prominent in the spectrum related to the optical measurement. Further, an assembly of peaks around 100 Hz was noticed in the spectrum of the reconstructed position, which was hardly present in the piezo sensor data used as a reference, causing the aforementioned modulation. The two observations were attributed to the fact that the built-in piezo stage sensor only measures displacements of the moveable part of the stage with respect to its housing. In contrast, the optical measurement is also sensitive to relative displacements between excitation field (focused beam) and particle. A second reason for the deviations was the higher noise level of the internal sensor of the positioning stage in the considered frequency range compared to the optical method. After applying a bandstop filter spanning the interval $[50 \text{ Hz}, 150 \text{ Hz}]$, both position data were again overlapped, resulting in an even better overlap. The serrated shape of the piezo data mainly resulted from the limited resolution of the built-in sensor. After this demonstration of the general applicability of the quadrant

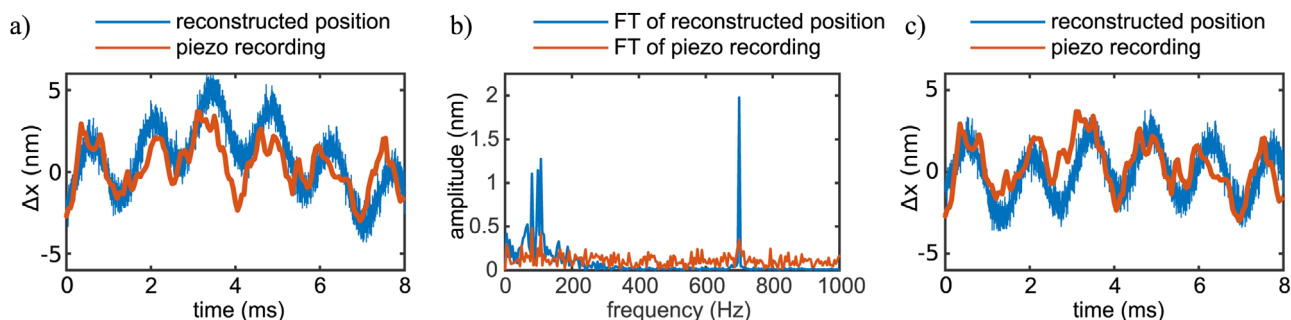


Figure 5. Excitation of an oscillation with a well-defined frequency using a vibration-generating source while simultaneously recording the position optically (blue) and with the built-in sensor of the piezo stage (red). a) Unfiltered time-dependent position data $x(t)$. b) Fourier spectra of both $x(t)$ datasets and c) improved overlap of both datasets after application of bandstop frequency filter in the range of [50 Hz, 150 Hz].

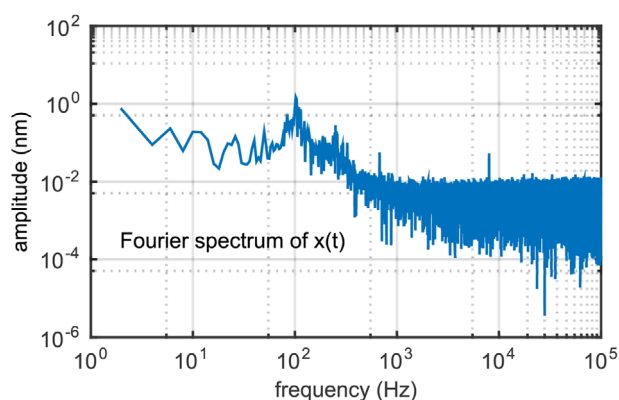


Figure 6. Fourier spectrum of the time-resolved position data $x(t)$. A particle oscillation with a frequency of 8 kHz is purposely excited in the setup and detected with the quadrant photodiode. The log-log plot clearly features a peak in the spectrum, which corresponds to the excited oscillation.

detection scheme to the Kerker based localization technique, the aim was to determine the full experimental capabilities in terms of detection speed. Oscillations of increasing frequency were externally excited to the setup and the attempt was to detect them by tracking the particle position via the time signals and their Fourier transform. The limits obtained in this proof-of-concept study were by no means ultimate, but rather defined by the coupling strength of external vibration source to the particle (on its substrate). The coupling efficiency strongly decreased for higher frequencies. Technically, up to sub-millisecond temporal steps of the data recording (125 μ s) were tested, which is equivalent to a limiting frequency of 8 kHz as shown in **Figure 6** in a log-log plot. The maximum detection speed obtained with the described approach already exceeds the frame rate of cameras of comparable cost. Furthermore, the optical method presented here outperforms the piezo-internal sensor, which does not allow anymore the retrieval of this highly frequent motion of the particle (or the stage). However, with the measured 8 kHz, the fundamental technical limit had not been reached, which would be ultimately set by the detector bandwidth and equals ~ 300 kHz for the detector utilized here. In addition to this remarkable temporal resolution, the method also provided quite a high spatial resolution. In order to determine the spatial resolution achieved in this proof-of-concept study, a calibration map was

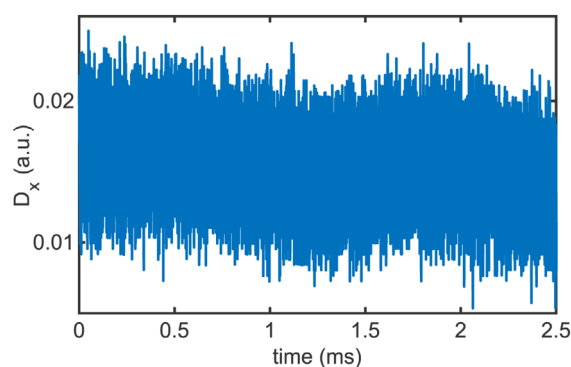


Figure 7. Calculation of spatial resolution. The plot shows a temporal section of the time-resolved directivity $D_x(t)$, leading to an estimate for the measurement uncertainty.

again considered for a particle displacement along the x -axis as described above. From this map, shown in **Figure 4**, the maximum change in directivity $\Delta D_{x,y}$ per nanometer displacement of the particle was read. A value of $\Delta D_{x,y} = 0.41\%$ was obtained for both directivity parameters. The noise level of the acquired signal was obtained from the unprocessed time-resolved directivity parameters $D_x(t), D_y(t)$. The corresponding data (for D_x only) are shown in **Figure 7**. Both parameters for the system were recorded without any additional external source of vibrations and the fluctuations of the directivity around the mean value (standard deviation σ) were considered. Owing to the fact that the amplitude of the fluctuations could be substantially reduced by a modification of the photodetector signal amplification in the course of the experiments, the major part of it was attributed to the QD and its amplifier. The described approach led to an estimate for a 2σ -noise level of $\delta D_x = 0.46\%$ and $\delta D_y = 0.42\%$. Ultimately, the experimentally achievable spatial resolution could be computed by dividing the uncertainty $\delta D_{x,y}$ by the signal strength $\Delta D_{x,y}$ for both parameters individually. A spatial resolution of $\delta x = \delta D_x / \Delta D_x = 1.1$ nm in x direction and $\delta y = \delta D_y / \Delta D_y = 1.0$ nm in y direction was reached. This localization precision was about one order of magnitude worse than the one achieved in previous camera-based experiments.^[19] However, the obtained values were hardly comparable, because the definition of localization precision differs substantially among the two studies. In ref. [19], the resolution is calculated

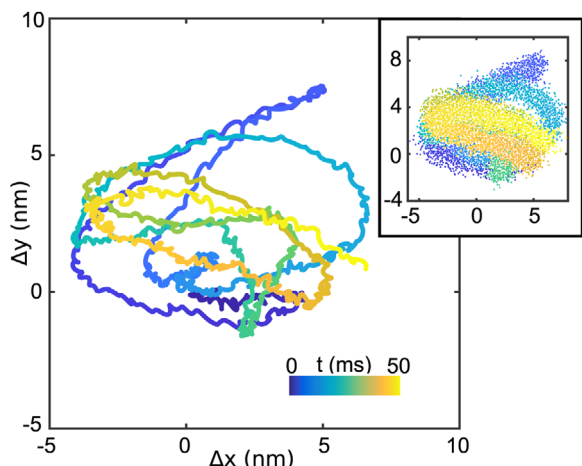


Figure 8. Trajectory of the silicon nanoparticle for a time interval of 50 ms. The plots show the relative position $\Delta x(t) = x(t) - x(t = 0)$ and $\Delta y(t) = y(t) - y(t = 0)$. We plot both the position data after application of a low-pass filter with a cut-off frequency of 8 kHz as well as the unaltered position data (inset). The color code indicates the temporal evolution.

using the pixel intensity distribution in differential BFP camera images, leading to an estimate of the stochastic uncertainty. The definition via single camera images necessarily includes time-averaging. In the present study, the time-resolved detection of the parameters calls for a different measure of uncertainty and resolution via the described signal-to-noise approach.

The combination of high resolution in both the spatial and temporal domain further enables the tracking of particle motion in 2D over relatively long time periods. **Figure 8** shows the particle position for a total time interval of 50 ms. Here, two sets of data from the same measurement are plotted. The trajectory presented in Figure 8 represents the particle position after application of a low-pass filter with a cut-off frequency at 8 kHz, whereas the inset shows the unfiltered reconstructed position data. Therefore, the former represents a noise-reduced trajectory, whereas the latter indicates the measurement uncertainty. The color code visualizes the temporal evolution for both data sets. The data show the drift of the particle position on the order of several nanometers over time, superposed by smaller-scale oscillations and the aforementioned uncertainty of approximately one nanometer. The observed particle trajectory mainly results from thermally and mechanically induced motion within the setup. Here, the actual reconstruction of the particle position is performed in the post-processing of the recorded data. However, an instantaneous reconstruction (which is reasonable from a technical point of view) would enable 2D live tracking of the particle position with high spatial and temporal resolution. Taking the approach one step further, such live tracking also paves the way toward stabilization of positioning stages based on the compensation of the measured displacements via a feedback-loop.

5. Conclusion

In this work, we extended the localization scheme presented in previous studies to the high-speed regime. We experimentally

reach a spatial resolution of approximately one nanometer, comparable with other state-of-the-art localization techniques. The spatial accuracy is mainly limited by high-frequency electronic noise, resulting from the detector and the corresponding amplification circuit. Further, we experimentally demonstrate a temporal resolution of 8 kHz, which exceeds the frame rate of common low-cost cameras substantially and could only be achieved by specialized, expensive high-speed cameras. However, the aforementioned experimentally achieved temporal resolution is by no means a fundamental limit but rather a technical limitation. It results from the weak mechanical coupling of our high-frequency oscillation source to the setup components. The actual fundamental limit is set by the bandwidth of the photodetector. The bandwidth of common pin-type silicon photodiodes typically reaches several 100 kHz, strongly depending again on the amplification of the signal. Hence, both spatial and temporal resolution mainly depend on the employed off-the-shelf photodetector. The method can also be extended to non-spherical particles, opening up the possibility for lithographical manufacturing of resonant structures such as cylinders. In addition, more complex structures could enable a stronger directionality due to the contribution of higher-order multipolar resonances. The extension to metal nanoparticles is also possible by employing the properties of a transversely spinning dipole close to an interface.^[32,40]

In terms of possible applications, high-speed real-time tracking of the nanoparticle in combination with a feedback loop can serve as a sample stabilization mechanism via instantaneous compensation of the measured particle displacements with the piezo actuator.^[41] This enables reduction of noise in sensitive optical setups, mostly resulting from mechanical oscillations of individual components. The aforementioned integrated on-chip arrangement of both scatterer and detectors^[21,42–45] constitutes an easy-to-implement and compact solution for such a stabilization mechanism. Using a multi-particle setting or more sophisticated illumination fields instead of a single scatterer and a simple excitation beam would further render the implementation more flexible and powerful by extending its capabilities and making it entirely alignment-free.

Supporting Information

Supporting Information is available from the Wiley Online Library or from the author.

Acknowledgements

This work was supported by the European Commission Horizon 2020 research and innovation programme under the Future and Emerging Technologies Open Grant Agreement Super-Pixels No. 829116.

Conflict of Interest

The authors declare no conflict of interest.

Keywords

directional scattering, tight focusing, ultrafast nanolocalization, vector beams

Received: March 24, 2020

Revised: June 17, 2020

Published online:

- [1] A. Dupont, D. C. Lamb, *Nanoscale* **2011**, *3*, 4532.
- [2] S. M. Salapaka, M. V. Salapaka, *IEEE Control Systems Magazine* **2008**, *28*, 65.
- [3] S. W. Hell, J. Wichmann, *Opt. Lett.* **1994**, *19*, 780.
- [4] T. A. Klar, S. W. Hell, *Opt. Lett.* **1999**, *24*, 954.
- [5] S. T. Hess, T. P. Girirajan, M. D. Mason, *Biophys. J.* **2006**, *91*, 4258.
- [6] E. Betzig, G. H. Patterson, R. Sougrat, O. W. Lindwasser, S. Olenych, J. S. Bonifacino, M. W. Davidson, J. Lippincott-Schwartz, H. F. Hess, *Science* **2006**, *313*, 1642.
- [7] S. Weisenburger, B. Jing, A. Renn, V. Sandoghdar, *Proc. SPIE* **2013**, *8815*.
- [8] K. Lindfors, T. Kalkbrenner, P. Stoller, V. Sandoghdar, *Phys. Rev. Lett.* **2004**, *93*, 037401.
- [9] V. Jacobsen, P. Stoller, C. Brunner, V. Vogel, V. Sandoghdar, *Opt. Express* **2006**, *14*, 405.
- [10] P. Kukura, H. Ewers, C. Müller, A. Renn, A. Helenius, V. Sandoghdar, *Nat. Methods* **2009**, *6*, 923.
- [11] R. W. Taylor, R. G. Mahmoodabadi, V. Rauschenberger, A. Giessel, A. Schambony, V. Sandoghdar, *Nat. Photonics* **2019**, *1*.
- [12] F. Gittes, C. F. Schmidt, *Opt. Lett.* **1998**, *23*, 7.
- [13] A. Rohrbach, E. H. K. Stelzer, *J. Appl. Phys.* **2002**, *91*, 5474.
- [14] L. Nugent-Glandorf, T. T. Perkins, *Opt. Lett.* **2004**, *29*, 2611.
- [15] S. Quabis, R. Dorn, M. Eberler, O. Glöckl, G. Leuchs, *Opt. Commun.* **2000**, *179*, 1.
- [16] R. Dorn, S. Quabis, G. Leuchs, *Phys. Rev. Lett.* **2003**, *91*, 233901.
- [17] H. Rubinsztein-Dunlop, A. Forbes, M. V. Berry, M. R. Dennis, D. L. Andrews, M. Mansuripur, C. Denz, C. Alpmann, P. Banzer, T. Bauer, E. Karimi, L. Marrucci, M. Padgett, M. Ritsch-Marte, N. M. Litchinitser, N. P. Bigelow, C. R. Guzmán, A. Belmonte, J. P. Torres, T. W. Neely, M. Baker, R. Gordon, A. B. Stilgoe, J. Romero, A. G. White, R. Fickler, A. E. Willner, G. Xie, B. McMorrán, A. M. Weiner, *J. Opt.* **2016**, *19*, 013001.
- [18] M. Neugebauer, P. Woźniak, A. Bag, G. Leuchs, P. Banzer, *Nat. Commun.* **2016**, *7*, 11286.
- [19] A. Bag, M. Neugebauer, P. Woźniak, G. Leuchs, P. Banzer, *Phys. Rev. Lett.* **2018**, *121*, 193902.
- [20] S. Nechayev, J. S. Eismann, M. Neugebauer, P. Woźniak, A. Bag, G. Leuchs, P. Banzer, *Phys. Rev. A* **2019**, *99*, 041801.
- [21] A. Bag, M. Neugebauer, U. Mick, S. Christiansen, S. A. Schulz, P. Banzer, *arXiv:1909.04478* **2019**.
- [22] S. Roy, K. Ushakova, Q. van den Berg, S. Pereira, H. Urbach, *Phys. Rev. Lett.* **2015**, *114*, 103903.
- [23] M. Kerker, D. S. Wang, C. Giles, *JOSA* **1983**, *73*, 765.
- [24] R. Alaei, R. Filter, D. Lehr, F. Lederer, C. Rockstuhl, *Opt. Lett.* **2015**, *40*, 2645.
- [25] B. García-Cámara, R. A. de La Osa, J. Saiz, F. González, F. Moreno, *Opt. Lett.* **2011**, *36*, 728.
- [26] J. M. Geffrin, B. García-Cámara, R. Gómez-Medina, P. Albella, L. Froufe-Pérez, C. Eyraud, A. Litman, R. Vaillon, F. González, M. Nieto-Vesperinas, J. J. Sáenz, F. Moreno, *Nat. Commun.* **2012**, *3*, 1171.
- [27] M. F. Picardi, A. V. Zayats, F. J. Rodríguez-Fortuno, *Phys. Rev. Lett.* **2018**, *120*, 117402.
- [28] S. Person, M. Jain, Z. Lapin, J. J. Sáenz, G. Wicks, L. Novotny, *Nano Lett.* **2013**, *13*, 1806.
- [29] M. Decker, I. Staude, M. Falkner, J. Dominguez, D. N. Neshev, I. Brener, T. Pertsch, Y. S. Kivshar, *Adv. Opt. Mater.* **2015**, *3*, 813.
- [30] T. Bauer, S. Orlov, U. Peschel, P. Banzer, G. Leuchs, *Nat. Photonics* **2014**, *8*, 23.
- [31] B. Richards, E. Wolf, *Proceedings of the Royal Society of London. Series A. Mathematical and Physical Sciences* **1959**, *253*, 358.
- [32] M. Neugebauer, T. Bauer, P. Banzer, G. Leuchs, *Nano Lett.* **2014**, *14*, 2546.
- [33] A. Aiello, P. Banzer, M. Neugebauer, G. Leuchs, *Nat. Photonics* **2015**, *9*, 789.
- [34] M. Nieto-Vesperinas, J. Sáenz, R. Gómez-Medina, L. Chantada, *Opt. Express* **2010**, *18*, 11428.
- [35] M. Neugebauer, J. S. Eismann, T. Bauer, P. Banzer, *Phys. Rev. X* **2018**, *8*, 021042.
- [36] P. Woźniak, P. Banzer, G. Leuchs, *Laser Photonics Rev.* **2015**, *9*, 231.
- [37] L. Marrucci, C. Manzo, D. Paparo, *Phys. Rev. Lett.* **2006**, *96*, 163905.
- [38] U. Mick, P. Banzer, S. Christiansen, G. Leuchs, *CLEO: Science and Innovations* **2014**, STu1H.
- [39] J. W. Cooley, J. W. Tukey, *Mathematics of Computation* **1965**, *19*, 297.
- [40] M. Neugebauer, S. Nechayev, M. Vorndran, G. Leuchs, P. Banzer, *Nano Lett.* **2019**, *19*, 422.
- [41] A. R. Carter, G. M. King, T. A. Ulrich, W. Halsey, D. Alchenberger, T. T. Perkins, *Appl. Opt.* **2007**, *46*, 421.
- [42] B. R. Watts, Z. Zhang, C. Q. Xu, X. Cao, M. Lin, *Biomedical Opt. Express* **2013**, *4*, 1051.
- [43] I. Luxmoore, N. Wasley, A. Ramsay, A. Thijssen, R. Oulton, M. Hugues, S. Kasture, V. Achanta, A. Fox, M. Skolnick, *Phys. Rev. Lett.* **2013**, *110*, 037402.
- [44] I. Luxmoore, N. Wasley, A. Ramsay, A. Thijssen, R. Oulton, M. Hugues, A. Fox, M. Skolnick, *Appl. Phys. Lett.* **2013**, *103*, 241102.
- [45] B. Le Feber, N. Rotenberg, L. Kuipers, *Nat. Commun.* **2015**, *6*, 6695.